Electronic Supplementary Material (ESI) for Materials Advances.
This journal is © The Royal Society of Chemistry 2021

Supporting Information for

Sulfur promotes hydrogen evolution on molybdenum carbide catalysts

Ju Ye Kim,[a,b,c,d] Per Lindgren,[a] Yin-Jia Zhang,[e] Seok Ki Kim,[d] Thomas M. Valentin,[a] Hee-tae Jung,[b,c] and Andrew A. Peterson[a]*

[a] School of Engineering, Brown University, Providence, Rhode Island, 02912, United States

[b] Department of Chemical and Biomolecular Engineering, Korea Advanced Institute of Science and Technology (KAIST), Daejeon, 34141, South Korea

[c] KAIST Institute for the NanoCentury, KAIST, 291 Daehak-ro, Yuseong-gu, Daejeon 34141, Republic of Korea

[d] Carbon Resources Institute, Korea Research Institute of Chemical Technology, 141 Gajeongro, Yuseong, Daejeon, Korea.

[e] Department of Chemistry, Brown University, Providence, Rhode Island, 02912, United States

Table of contents:

1. Electronic structure calculations

Electronic structure calculations were conducted for clean and sulfur-doped Mo_2C surfaces. Herein, we investigate the preferred adsorption sites of sulfur and hydrogen on Mo_2C, and the effect sulfur coverage has on the hydrogen binding energy on Mo_2C.

Adsorption on bare Mo_2C

The Mo_2C slab has five different adsorption sites:

- top
- bridge
- hollow site with subsurface molybdenum
- hollow site with subsurface carbon
- hollow site with subsurface vacancy

The hollow sites are labeled in Fig. 1a, which shows the unit cell of the Mo_2C system.

The hollow site with a subsurface vacancy was the preferred hydrogen adsorption site on clean Mo_2C. This is reasonable, since the size of hydrogen prevents any energetic penalties associated with steric hindrance in the hollow site. The bridge site adsorption was not stable; the hydrogen moved to one of the adjacent hollow sites during structural relaxation.

Sulfur adsorption on Mo_2C

To study the effect of sulfur doping on the hydrogen binding energy of Mo_2C, we adsorbed sulfur onto the slab with varying coverages ($0 \leq \theta_S \leq 1$). For sulfur coverages of $\theta_S = 0.25$ and $\theta_S = 0.50$ the preferred adsorption sites are hollow sites with subsurface vacancy. However, for coverages

$\theta_S \geq 0.75$ there are no available hollow site with subsurface vacancy. The sulfur atoms therefore adsorb in hollow sites with subsurface carbon (see Fig. 1c). These results are in qualitative agreement with the XPS results in Fig. 4, which suggest that there is no C-S binding for low and intermediate sulfur loadings (≤ 7.2 wt%), but there is C-S binding for higher sulfur loadings (≥ 11 wt%).

Effect of sulfur coverage on H adsorption on Mo_2C

Hydrogen binding energies on Mo_2C with sulfur coverages of $\theta_S = 0.25$, $\theta_S = 0.50$, $\theta_S = 0.75$ and $\theta_S = 1.0$ were calculated to study the effect of sulfur coverage. The hydrogen adsorption sites for varying coverages are shown in Fig. 1c. For low sulfur coverages, the hollow site with subsurface vacancy is the most stable hydrogen adsorption site. However, as the sulfur coverage increases, the hydrogen must adsorb in a hollow site with subsurface carbon ($\theta_S = 0.50$ and $\theta_S = 0.75$) or subsurface molybdenum ($\theta_S = 1.0$). This introduces a significant energetic penalty, which is evident in Fig. 1c.

Fig. 1b shows the free energy diagram of hydrogen adsorption on Mo_2C for various sulfur coverages. The free energy of adsorption on a bare Mo_2C surface was -0.72 eV; Mo_2C thus binds hydrogen strongly. Sulfur coverage has a significant effect on the hydrogen binding energy. This is less pronounced for $\theta_S = 0.25$, where hydrogen can still adsorb in a hollow site with subsurface vacancy. For higher sulfur coverages, however, hydrogen must adsorb in an energetically unfavorable site, causing the hydrogen binding energy to decrease. Our results indicate that Mo_2C with intermediate sulfur coverage ($\theta_S = 0.50$ and $\theta_S = 0.75$) exhibits close to thermoneutral hydrogen binding energy. Lower ($\theta_S = 0$ and $\theta_S = 0.25$) and higher ($\theta_S = 1.0$) sulfur coverages bind

hydrogen too strongly and too weakly, respectively. Overall, the sulfur on Mo_2C with intermediate coverage (θ_S = 0.50 and θ_S = 0.75) effectively acts as “long-lasting poison" introducing an undesired hydrogen adsorption site by occupying the original hydrogen adsorption sites instead. And thus “long-lasting poison" performs as “catalyst promoters" facilitating the HER activity with shifting the HER volcano position toward the top.

2. Fabrication procedure for sulfur-doped molybdenum carbide

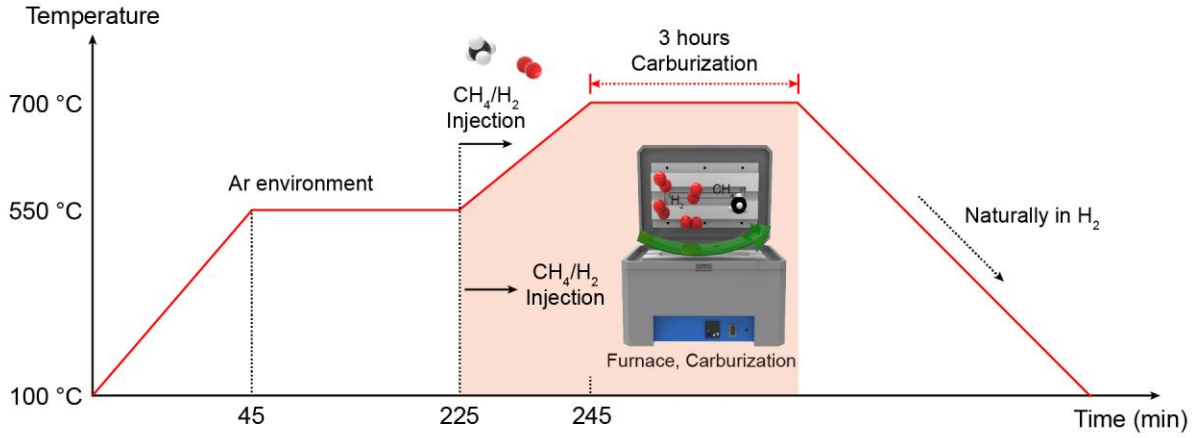

Fig. S1. Experimental condition of temperature programmed reduction (TPR) process. X-axis represents reaction time and y-axis shows reaction temperature.

Fig. S1 shows the overall fabrication procedure. Aqueous solutions of molybdenum (Mo), urea and sulfur salt were prepared at 25 °C with stirring. After all the precursors were dissolved (with each desired ratio of Mo:S), the solution was placed into an oil bath at 90 °C in a sealed bottle producing alkoxide compounds. Six hours later, the compound solution was evaporated in 110 °C oven overnight. The final compound powder was placed into a tubular furnace under an Ar gas environment until the temperature was heated up to 550 °C. For the next carburization process, H_2/CH_4 mixture gases were introduced while heating the temperature up to 700 °C. Here, CH_4 is a carbon source for synthesizing Mo_2C from Mo salt. The final products were cooled down naturally in an H_2 environment.

3. Inductively coupled plasma atomic emission spectroscopy (ICP-AES)

Table S1. ICP results for the prepared catalysts; Mo_2C, S(1), S(7), and S(11)

Materials	Mo salt 102mg + S salt X mg	S wt %
Mo_2C	0	0
S(1)	9.7	1.1
S(7)	38	7.2
S(11)	58	11.1

The weight percent of sulfur was determined by ICP-AES results, confirming the successful sulfur insertion into Mo_2C.

4. Low-magnification SEM image of sulfur-doped molybdenum carbide (7 wt%)

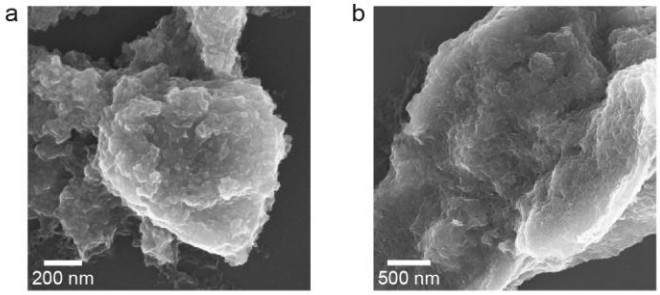

Fig. S2. (a-b) Morphology investigation with scanning electron microscopy (SEM) of 7 wt% sulfur doped molybdenum carbide (S(7)) with different magnifications.

As the sulfur doping concentrations increased, the particle shape of Mo_2C was changed into a sheet-like morphology. Fig. S2 shows the shape of the 7.2-wt% sulfur-doped Mo_2C (S(7)) catalyst at lower magnifications.

5. Pore size distribution, BET surface area, BJH pore volume and average pore diameter

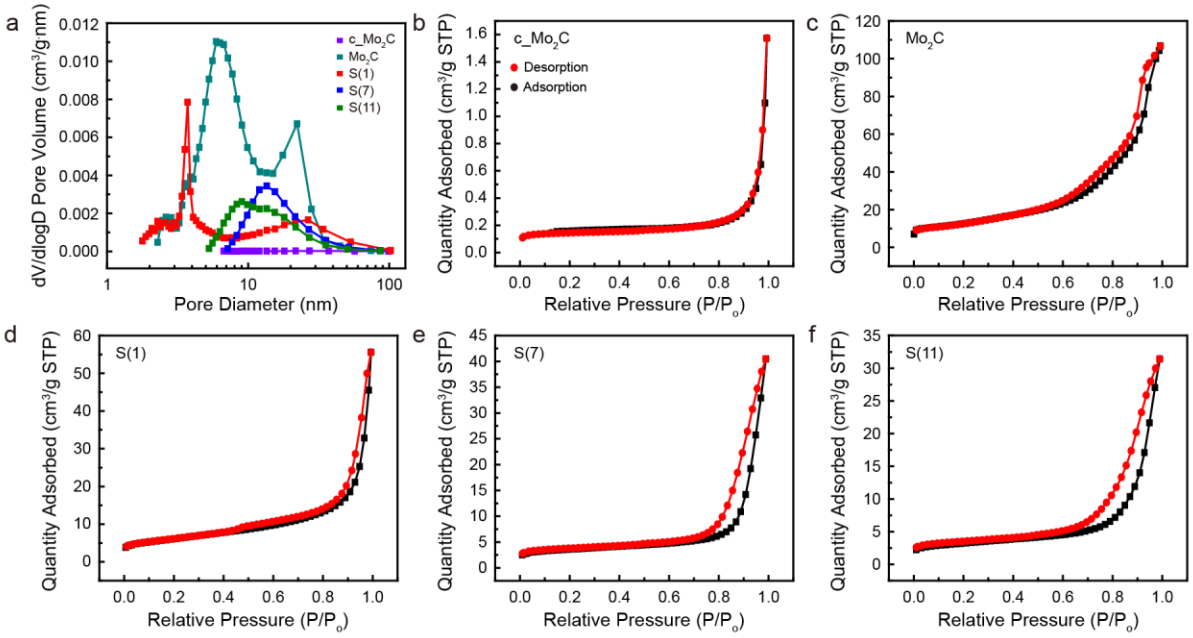

Fig. S3. (a) BET surface area, BJH pore volume and average pore diameter pore size distributions of synthesized molybdenum carbides (represented as differential pore volume against log scale of pore diameter). (b-f) Nitrogen adsorption and desorption isotherm linear plot by Brunauer-Emmett-Teller (BET) model for various sulfur loaded molybdenum carbides.

Table S2. Brunauer-Emmett-Teller (BET) surface area, Barrett-Joyner-Halenda (BJH) pore volume, and pore size information

Materials	BET surface area (m^2/g)	Pore Volume (cm^3/g)	Average Pore Diameter (nm)
c_Mo_2C	0.6031	0.002324	46.2534
Mo_2C	44.0782	0.171089	11.7959
S(1)	21.5627	0.085186	17.0511
S(7)	12.9432	0.065190	19.1710
S(11)	11.4953	0.049992	15.5234

To verify the porous structure and understand the distribution of pores in synthesized catalysts, the Brunauer–Emmett–Teller(BET) and Barrett–Joyner–Halenda(BJH) methods were employed, the results are shown in Fig. S3 and Table S1. 0.1g of each sample was prepared for the analysis. The commercial Mo_2C (labeled as c_Mo_2C) was prepared for comparison, and as expected, the near-zero pore volume and the corresponding low surface area were observed. On the contrary, our

synthesized Mo_2C had the highest surface area with large pore volumes. As the sulfur concentration increased, the shape of catalysts was changed towards a sheet morphology (as shown in the SEM analysis of Fig. 2). This corresponds to a decrease in surface area with sulfur doping in the BET analysis.

6. Supporting calculations about the lattice d-spacing and related angular

From the XRD analysis, not only the crystal system but also the real distance information was obtained from each unit cell of the catalyst. Theoretical distances in each plane for the orthorhomic structure were calculated as shown below to compare with the measured lattice fringe distances of the catalysts from the HR-TEM analysis. Here, d-spacings from HR-TEM were measured by averaging more than 10 lattice distances. This suggested that the surfaces were (020) and (211), respectively. We also confirmed that the theoretical value and the measured value in the actual experiment corresponded to each other by calculating the angular distance between the two planes, proving that the surface was Mo_2C of the orthorhombic structure.

$$a \neq b \neq c; a = 6.041758\ \text{Å}, b = 4.745728\ \text{Å}, c = 5.214426\ \text{Å}$$

$$\alpha = \beta = \gamma = 90\ °$$

$$|\overrightarrow{a*}| = \frac{1}{a}\ , |\overrightarrow{b*}| = \frac{1}{b}\ , |\overrightarrow{c*}| = \frac{1}{c}$$

$$d_{hkl} = \frac{1}{\sqrt{(\frac{h}{a})^2 + (\frac{k}{b})^2 + (\frac{l}{c})^2}}$$

$$d_{020} = \frac{1}{\sqrt{(\frac{2}{4.745728})^2}} = 2.37\ \text{Å}$$

$$d_{211} = \frac{1}{\sqrt{(\frac{2}{6.041758})^2 + (\frac{1}{4.745728})^2 + (\frac{1}{5.214426})^2}} = 2.29\ \text{Å}$$

$$\cos \emptyset = \frac{\frac{h_1 h_2}{a^2} + \frac{k_1 k_2}{b^2} + \frac{l_1 l_2}{c^2}}{\sqrt{(\frac{h_1}{a})^2 + (\frac{k_1}{b})^2 + (\frac{l_1}{c})^2}\sqrt{(\frac{h_2}{a})^2 + (\frac{k_2}{b})^2 + (\frac{l_2}{c})^2}}$$

$$\cos \emptyset = \frac{\frac{2}{b^2}}{\sqrt{(\frac{2}{b})^2}\sqrt{(\frac{2}{a})^2 + (\frac{1}{b})^2 + (\frac{1}{c})^2}} = 0.48245 \text{ Å}$$

$$\emptyset = 61.15 \text{ °}$$

7. HR-TEM image observations for 11 wt% sulfur-doped Mo_2C

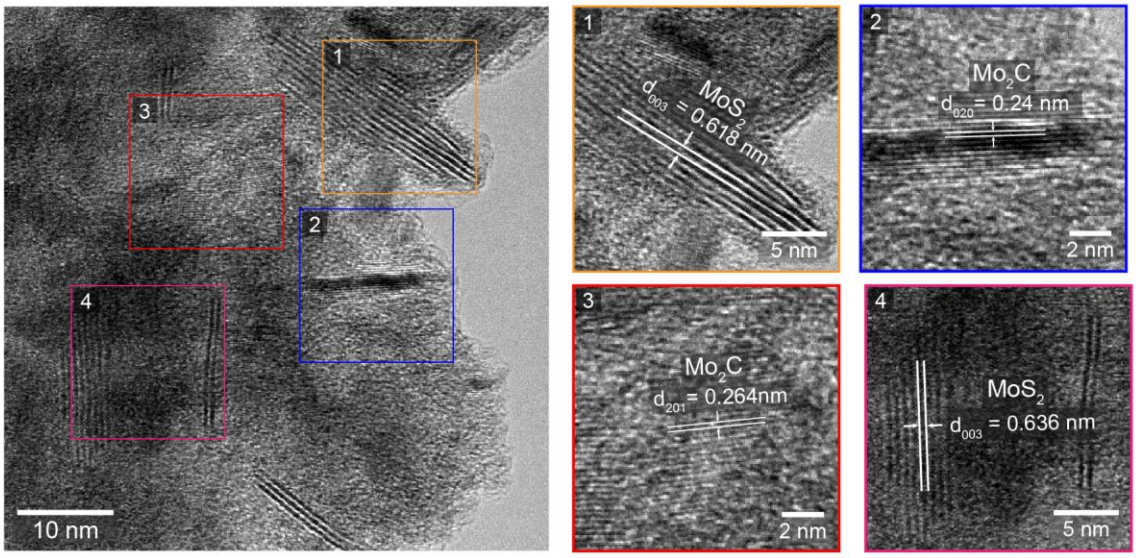

Fig. S4. HRTEM image of higher sulfur loadings Mo_2C (11 wt%); point 1 and 4 refer to MoS_2 lattice while point 2 and 3 show Mo_2C fringes

To further observe the structure of (excessively) sulfur-doped Mo_2C catalysts, HR-TEM analysis was carried out. The distances were measured to be 0.618 nm and 0.636 nm, which are consistent with (002) plane of molybdenum disulfide (point 1 and 4 in Fig. S4). The other two lattice distances (point 2 and 3 in Fig. S4) were calculated as 0.24 nm and 0.264 nm, which correspond most closely to (020) and (201) planes of molybdenum carbide, respectively. Consistent with the XRD results in Fig. 3, we confirmed the complex of typical d-spacing of MoS_2 and Mo_2C; point 2 and 3 represent Mo_2C area while point 1 and 4 show MoS_2, respectively.

8. Characterization of the synthesized Mo_2C (porous, non-sulfur doped)

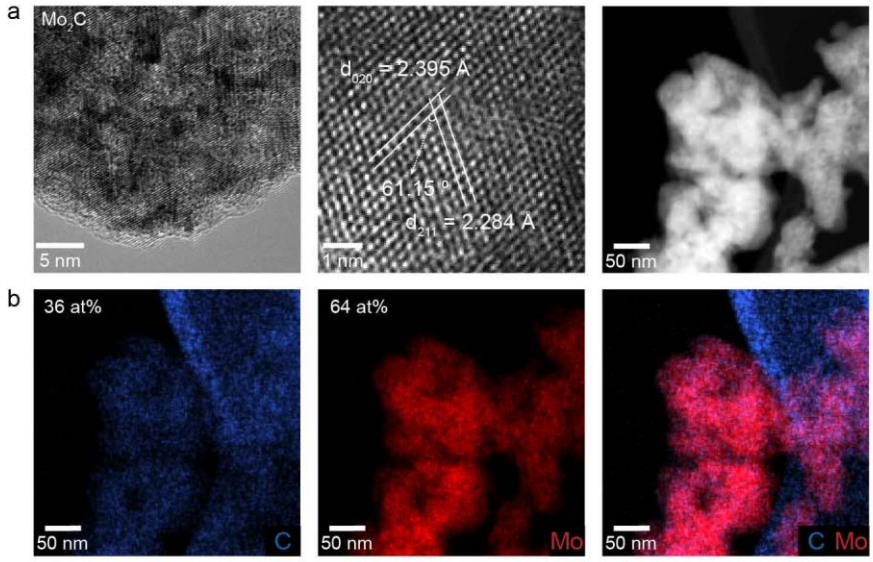

Fig. S5. Characterizations of the synthesized Mo_2C. (a) HR-TEM and STEM image and (b) EDS mapping results.

The characterizations of the non-sufur doped porous Mo_2C were represented in Fig. S5. The lattice distance and related angular were matched with the typical properties of Mo_2C. A scanning transmission electron microscope (STEM) shows the porous features of Mo_2C. EDS mapping supports the uniform distribution of Mo and C.

9. Raman observations range from 100 cm^{-1} to 500 cm^{-1}

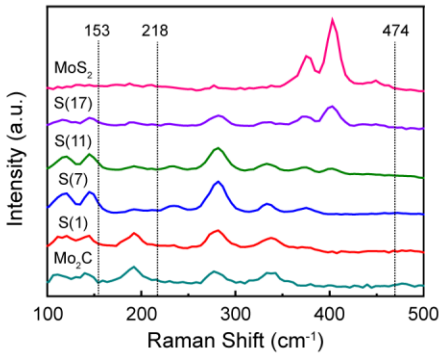

Fig. S6. Raman spectroscopy observations in a range from 100 to 500 cm^{-1} for Mo_2C, S(1), S(7), S(11), S(17) and MoS_2.

To observe whether an aggregated sulfur was formed by S-S bonds instead of inserting sulfur into the Mo_2C crystal structure, a Raman peak range from 100 cm^{-1} to 500 cm^{-1} (which is a typical sulfur peak range) was shown in Fig. S6. All the prepared samples did not show sulfur peaks (153, 218 and 474 cm^{-1}), indicating that there was no formation of aggregated sulfur. Thus, it can be assumed that sulfur was only used for doping into Mo_2C or to generate MoS_2.

10. The Raman optical microscope images of fabricated catalysts

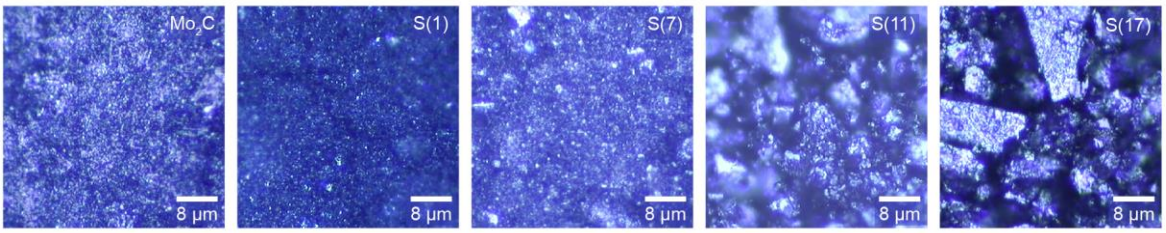

Fig. S7. The Raman optical microscope images of as-synthesized catalysts : Mo_2C, 1 wt% sulfur doped Mo_2C, 7 wt% sulfur doped Mo_2C, 11 wt% sulfur doped Mo_2C, and 17 wt% sulfur doped Mo_2C

Fig. S7 shows the bulk morphology of all the synthesized catalysts using the Raman optical microscope. From the sulfur doping concentration of 11 wt%, large MoS_2 islands were formed in agreement with Fig. S4.

11. XPS peak table

Table S3. Binding energies of C 1s and S 2p (eV) for synthesized catalysts

	C 1s					S 2p				
Catalysts	C-Mo	C-C	C-O	C-S	O-C=O	S-Mo ($2p_{3/2}$)	S-Mo ($2p_{1/2}$)	S-C ($2p_{3/2}$)	S-C ($2p_{1/2}$)	SO_4^{2-}
Mo_2C	284.11	284.7	286.08	-	288.57	-	-	-	-	-
S(1)	283.75	284.7	286.01	-	288.52	162.05	163.35	-	-	-
S(7)	283.64	284.7	286.06	-	288.64	162.13	163.23	-	-	168.78
S(11)	283.79	284.7	286.08	285.67	288.64	162.14	163.24	162.23	163.53	168.95

Table S3 shows binding energies of C 1s, N 1s and S 2p spectra for all synthesized catalysts.

12. Cyclic voltammetry (CV) in a non-faradaic region

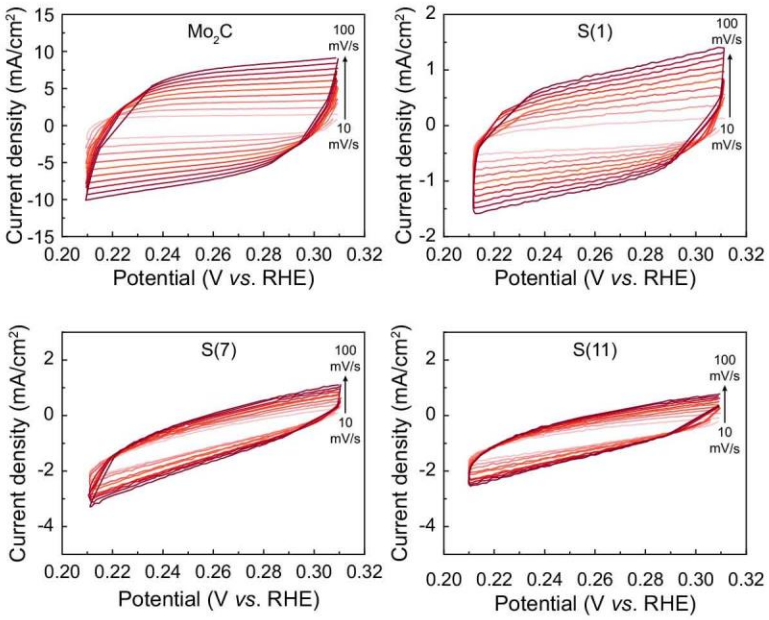

Fig. S8. Cyclic voltammetry (CV) results in a non-faradaic region for Mo_2C, S(1), S(7), and S(11). Scan rates were 10, 20, 30, 40, 50, 60, 70, 80, 90, and 100 mV/s.

To estimate the electrochemical surface area (ECSA), cyclic voltammetry (CV) test was performed in the non-faradaic region with a scan rate range of 10 mV/s to 100 mV/s. Based on Fig. S8, double-layer capacitance (C_{dl}) of each catalyst was calculated and then represented in Fig. S9.

13. Electrochemical double layer capacitance (C_{dl})

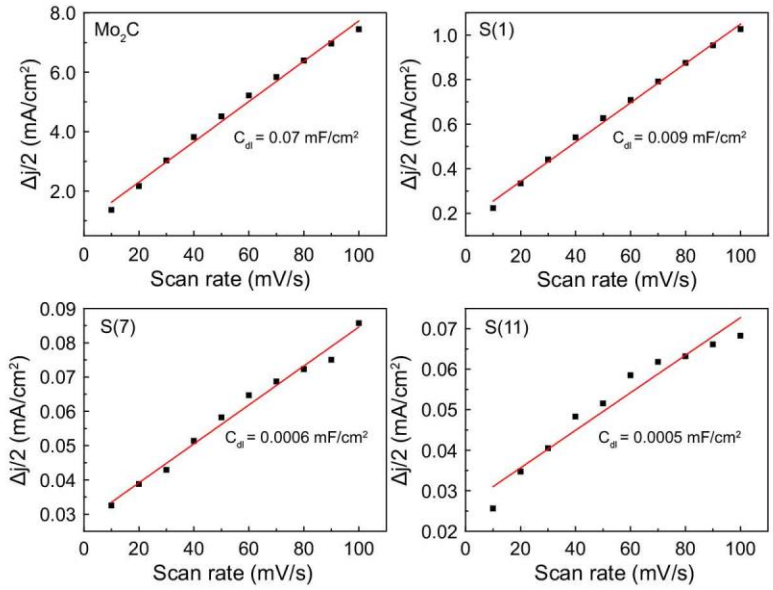

Fig. S9. The double-layer capacitance results for Mo_2C, S(1), S(7), and S(11).

From Fig S8, $\Delta j/2 = |j_a - j_c|/2$ was plotted against the scan rate. The slope represents the double layer capacitance (C_{dl}) as written in graphs. Electrochemical surface area (ECSA) can be calculated following the equation : $ECSA = \frac{C_{dl}}{C_s}$, where C_s stands for the specific capacitance.

Let's assume that C_s is $35\mu F/cm_{ECSA}^2$ in 0.5M H_2SO_4.

Then the ECSA of catalysts were 2, 0.26, 0.017, 0.014 for the Mo_2C, S(1), S(7), and S(11), respectively.

14. LSV based on ECSA and BET

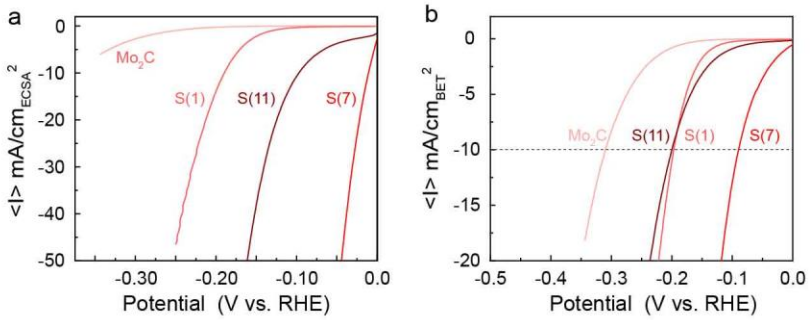

Fig. S10. Polarization curves based on (a) ECSA and (b) BET surface area.

To investigate the intrinsic activity, the LSV graph in Fig. 5a was re-plotted based on the ECSA and BET from Fig. S8-S9 and Fig. S3, respectively.

15. State-of-arts hydrogen evolution reaction using molybdenum carbide-based catalysts

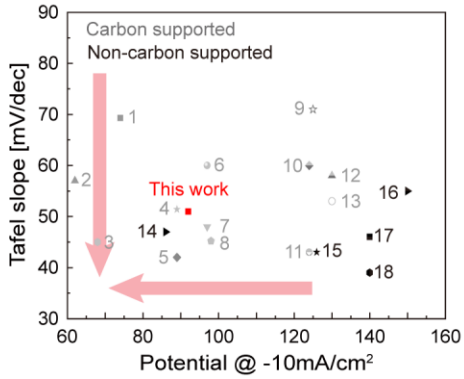

Fig. S11. Comparison of Tafel slope (y axis) and overpotential at -10 mA/cm^2 with previously reported works. From 1 to 13, it refers carbon supported catalyst group whereas from 14 to 18 shows non-carbon supported catalyst group[1-18]

When we comparing our catalyst performance with previously reported electrocatalyst (Fig. S11), it can be seen that it is comparable to the recently reported excellent catalysts. Especially, among the catalyst which did not use any carbon support, it was the second best performance. Since it is well known that the performance of the catalyst can be improved when there is carbon support, we can expect the further improvements of our sulfur-doped Mo_2C catalyst by adding carbon support.

16. References

1. X. Luo, Q. Zhou, S. Du, J. Li, J. Zhong, X. Deng and Y. Liu, *ACS Appl. Mater. Interfaces*, 2018, **10**, 22291-22302.
2. Z. Zhou, Z. Yuan, S. Li, H. Li, J. Chen, Y. Wang, Q. Huang, C. Wang, H. E. Karahan, G. Henkelman, X. Liao, L. Wei and Y. Chen, *Small*, 2019, **15**, e1900358.
3. S. Wang, J. Wang, M. Zhu, X. Bao, B. Xiao, D. Su, H. Li and Y. Wang, *J. Am. Chem. Soc.*, 2015, **137**, 15753-15759.
4. H. Zhang, Z. Ma, G. Liu, L. Shi, J. Tang, H. Pang, K. Wu, T. Takei, J. Zhang, Y. Yamauchi and J. Ye, *NPG Asia Mater.*, 2016, **8**, e293-e293.
5. Z. Shi, K. Nie, Z.-J. Shao, B. Gao, H. Lin, H. Zhang, B. Liu, Y. Wang, Y. Zhang, X. Sun, X.-M. Cao, P. Hu, Q. Gao and Y. Tang, *Energy Environ. Sci.*, 2017, **10**, 1262-1271.
6. H. Ang, H. Wang, B. Li, Y. Zong, X. Wang and Q. Yan, *Small*, 2016, **12**, 2859-2865.
7. Z. Xu, G. Zhang, C. Lu, H. Tian, X. Xi, R. Liu and D. Wu, *J. Mater. Chem. A*, 2018, **6**, 18833-18838.
8. J.-S. Li, Y.-J. Tang, C.-H. Liu, S.-L. Li, R.-H. Li, L.-Z. Dong, Z.-H. Dai, J.-C. Bao and Y.-Q. Lan, *J. Mater. Chem. A*, 2016, **4**, 1202-1207.
9. Y. Ma, M. Chen, H. Geng, H. Dong, P. Wu, X. Li, G. Guan and T. Wang, *Adv. Funct. Mater.*, 2020, **30**.
10. Y. Liu, G. Yu, G. D. Li, Y. Sun, T. Asefa, W. Chen and X. Zou, *Angew. Chem. Int. Ed.*, 2015, **54**, 10752-10757.
11. Z. Shi, Y. Wang, H. Lin, H. Zhang, M. Shen, S. Xie, Y. Zhang, Q. Gao and Y. Tang, *J. Mater. Chem. A*, 2016, **4**, 6006-6013.
12. D. H. Youn, S. Han, J. Y. Kim, J. Y. Kim, H. Park, S. H. Choi and J. S. Lee, *ACS Nano*, 2014, **8**, 5164-5173.
13. L. Liao, S. Wang, J. Xiao, X. Bian, Y. Zhang, M. D. Scanlon, X. Hu, Y. Tang, B. Liu and H. H. Girault, *Energy Environ. Sci.*, 2014, **7**, 387-392.
14. H. Ang, H. T. Tan, Z. M. Luo, Y. Zhang, Y. Y. Guo, G. Guo, H. Zhang and Q. Yan, *Small*, 2015, **11**, 6278-6284.
15. H. Lin, Z. Shi, S. He, X. Yu, S. Wang, Q. Gao and Y. Tang, *Chem. Sci.*, 2016, **7**, 3399-3405.
16. J. Dong, Q. Wu, C. Huang, W. Yao and Q. Xu, *J. Mater. Chem. A*, 2018, **6**, 10028-10035.
17. Y. Zhao, K. Kamiya, K. Hashimoto and S. Nakanishi, *J. Am. Chem. Soc.*, 2015, **137**, 110-113.
18. H. Lin, N. Liu, Z. Shi, Y. Guo, Y. Tang and Q. Gao, *Adv. Funct. Mater.*, 2016, **26**, 5590-5598.